A purely nonlinear route to transition approaching the edge of chaos in a boundary layer

S Cherubini[1], **P De Palma**[1], **J-Ch Robinet**[2] **and A Bottaro**[3]

[1] DIMeG and CEMeC, Politecnico di Bari, via Re David 200, 70125 Bari, Italy
[2] DynFluid, Arts et Métiers ParisTech, 151, Bd. de l'Hopital, 75013 Paris, France
[3] DICAT, Universitá di Genova, via Montallegro 1, 16145 Genova, Italy

E-mail: s.cherubini@gmail.com

Abstract

The understanding of transition in shear flows has recently progressed along new paradigms based on the central role of coherent flow structures and their nonlinear interactions. We follow such paradigms to identify, by means of a nonlinear optimization of the energy growth at short time, the initial perturbation which most easily induces transition in a boundary layer. Moreover, a bisection procedure has been used to identify localized flow structures living on the edge of chaos, found to be populated by hairpin vortices and streaks. Such an edge structure appears to act as a relative attractor for the trajectory of the laminar base state perturbed by the initial finite-amplitude disturbances, mediating the route to turbulence of the flow, via the triggering of a regeneration cycle of Λ and hairpin structures at different space and time scales. These findings introduce a new, purely nonlinear scenario of transition in a boundary-layer flow.

(Some figures may appear in colour only in the online journal)

1. Introduction

Recent progress in understanding the transition to turbulence has been boosted by a recently originated dynamical system view according to which transition and turbulence can be envisioned as the random walk of the system's trajectory among mutually repelling states, which are exact unstable solutions of the Navier–Stokes equations (Nagata 1997, Waleffe 1998, Faisst and Eckhardt 2003, Hof *et al* 2004, Eckhardt *et al* 2007). Some of these solutions, called *edge states*, live in the phase space on the boundary between the laminar and the turbulent attractors, acting as relative attractors for the states evolving along its stable

manifold (Skufca *et al* 2006). Evidence for the physical consistency of such a theory of chaos was found for the cases of pipe and Couette flows (Waleffe 1998, Eckhardt *et al* 2007). Many unstable nonlinear solutions have been identified, initially in small periodic domains and recently also in longer domains, where localized solutions have emerged (Schneider *et al* 2010). These solutions appear to be relevant for describing the features of the transition induced by disturbances that grow and eventually invade the flow in the form of turbulent spots.

On the other hand, for spatially developing flows such as the boundary layer, the analysis of the transition process has focused on linear receptivity and transient growth, motivating the search for optimal perturbations, defined as those initial flow states which elicit the largest energy growth over a given time or space interval (Farrell 1988, Luchini 2000). The rationale was that the linear amplification of an initial disturbance was sufficient to bootstrap the system towards a self-sustained, large-amplitude state, thus bypassing the long-time decay associated with the linear system's damped eigenmodes. Linear transient growth analyses have thus suggested that bypass transition relies on the generation of elongated streaks which undergo secondary instability and breakdown (Andersson *et al* 2001). Nonetheless, it has been shown that linear optimal disturbances are poor at triggering transition, in this being easily surpassed by suboptimal initial conditions (Biau and Bottaro 2009). Thus, it appears important to devise a *nonlinear* strategy capable of yielding the most dangerous *shape* and *amplitude* of the initial conditions which evolve towards nonlinear exact solutions such as those living on the edge of chaos (Viswanath and Cvitanovic 2009, Duguet *et al* 2010).

2. Method

In this work, we use an optimization procedure to determine the shape of the initial perturbation which leads, at finite time, close to the edge of chaos (in some energy norm). Typically, edge states are characterized by a finite perturbation energy, E_E, lower than that of the turbulent state, E_T. Thus, in order to map the state space in the vicinity of the edge of chaos, we look for the initial perturbation of initial energy E_0 which can induce at a target time T the largest disturbance energy (Farrell 1988, Luchini 2000) $E(t) = \langle \mathbf{u}(t) \cdot \mathbf{u}(t) \rangle$, where the symbol $\langle \rangle$ indicates integration over the considered three-dimensional domain and $\mathbf{u}$ is the disturbance velocity vector $\mathbf{u} = (u, v, w)^{\mathrm{T}}$. The initial *optimal perturbation* is computed by means of a Lagrange multiplier technique (see also Pringle and Kerswell (2010)), which consists in finding the extrema of the augmented functional

$$
\begin{aligned}
\mathcal{L} = \quad & \frac{E(T)}{E(0)} - \int_0^T \langle p^\dagger \nabla \cdot \mathbf{u} \rangle \, \mathrm{d}t - \int_0^T \left\langle \mathbf{u}^\dagger \cdot \left\{ \frac{\partial \mathbf{u}}{\partial t} + \mathbf{u} \cdot \nabla \mathbf{U} \right. \right. \\
& \left. \left. + \mathbf{U} \cdot \nabla \mathbf{u} + \mathbf{u} \cdot \nabla \mathbf{u} + \nabla p - \frac{\nabla^2 \mathbf{u}}{Re} \right\} \right\rangle \mathrm{d}t - \lambda \left(\frac{E_0}{E(0)} - 1 \right).
\end{aligned}
\tag{1}
$$

In equation (1), the constraints are the initial perturbation energy, $E_0 = \langle \mathbf{u}_0 \cdot \mathbf{u}_0 \rangle$, and the nonlinear Navier–Stokes equations in a perturbative formulation; $\mathbf{U}(x, y)$ is the Blasius base flow; p is the pressure perturbation and $(\mathbf{u}^\dagger, p^\dagger, \lambda)$ are the Lagrange multipliers needed to enforce the constraints. The Reynolds number is defined as $Re = U_\infty \delta^*/\nu$, where ν, δ^* and U_∞ are the kinematic viscosity, the inflow boundary-layer displacement thickness and the freestream velocity, respectively. A zero-perturbation condition has been imposed at inlet, outlet, bottom and upper boundary points, whereas periodicity is imposed in the spanwise homogeneous direction. A fringe region is used at the inlet and outlet points to let the perturbation vanish smoothly, the goal of the study being that of identifying localized

disturbances. Integrating by parts and setting to zero the first variation of $\mathcal{L}$ with respect to $(\mathbf{u}, p)$ leads to the adjoint equations plus the compatibility condition. The adjoint equations are linked to the direct ones by the presence of direct variables in the advection terms; thus, the whole direct field needs to be stored at each time step, requiring a very large storage capacity. By solving the direct and adjoint equations at each step of the iterative procedure, the first variation of the augmented functional with respect to $\mathbf{u}$, p and $\mathbf{u}^\dagger$, $p^\dagger$ is set to zero. Moreover, the gradient of $\mathcal{L}$ with respect to the initial state $\mathbf{u}_0$ has to vanish within a reasonable number of iterations. In order to achieve convergence efficiently, a conjugate gradient algorithm is used, similar to that employed in Marquet *et al* (2008). The initial state is updated in the steepest ascent direction, denoted as $\nabla_{\mathbf{u}_0}\mathcal{L}$, namely:

$$
\begin{aligned}
\frac{\partial \mathcal{L}}{\partial u_0} &= -2u_0 \frac{(E(T) - \lambda E_0)}{E(0)^2} + u^\dagger(0), \\
\frac{\partial \mathcal{L}}{\partial v_0} &= -2v_0 \frac{(E(T) - \lambda E_0)}{E(0)^2} + v^\dagger(0), \\
\frac{\partial \mathcal{L}}{\partial w_0} &= -2w_0 \frac{(E(T) - \lambda E_0)}{E(0)^2} + w^\dagger(0),
\end{aligned}
\tag{2}
$$

with an adjustable step length α, so that $\mathbf{u}_0^{(n+1)} = \mathbf{u}_0^n + \alpha^n \nabla_{\mathbf{u}_0}\mathcal{L}^n$. After the first iteration in the steepest ascent direction (with α sufficiently large for the solution to be significantly modified), the successive steps are taken along a conjugate direction, $\Lambda\mathbf{u}_0$, which is computed on the basis of the gradient at two consecutive iterations according to $\Lambda\mathbf{u}_0^{(n+1)} = \nabla_{\mathbf{u}_0}\mathcal{L}^{(n+1)} + \beta^{(n+1)} \Lambda\mathbf{u}_0^n$. In this work, the value of the parameter $\beta^{(n+1)}$ is computed by means of the Polak–Ribière formula (Polak and Ribière 1969). Periodically, this value should be reset to zero in order to avoid conjugacy loss (which corresponds to updating the solution in the steepest ascent direction). The step length α has been chosen carefully in order to ensure convergence to the optimal value, as described below, with values in the range $[0.001/E_0, 0.1/E_0]$. The optimization procedure for a chosen target time T can be summarized as follows:

(i) An initial guess is made for the initial condition, $\mathbf{u}_0$, with the associated initial energy E_0 (in most of the computations, the perturbation obtained by a linear optimization has been used as the initial guess).

(ii) The direct problem is integrated up to $t = T$.

(iii) The adjoint variables, $(\mathbf{u}^\dagger, p^\dagger, \lambda)$, are provided by the compatibility conditions.

(iv) The adjoint problem is integrated backward in time from $t = T$ to $t = 0$.

(v) At $t = 0$, the initial direct state is updated in the direction of the conjugate gradient with step length α and β computed according to the Polak–Ribière formula ($\beta = 0$ is imposed at the first iteration).

(vi) The objective function $E(T)$ is evaluated:

    (a) if its increase between two successive iterations is smaller than a chosen threshold, e, the loop is stopped; otherwise the procedure is continued from step (ii);

    (b) if a decrease of the objective function is found, the value of α is halved, and the value of β is set to zero.

A threshold value equal to $e = 10^{-6}$ has been chosen (a more detailed convergence study is given in Cherubini *et al* (2010)). The direct equations and the dual system are integrated by a second-order-accurate fractional step method (Verzicco and Orlandi 1996). A domain with $L_x = 200$, $L_y = 20$ and $L_z = 10.5$ has been chosen, x, y and z being the streamwise, the wall-normal and the spanwise direction, respectively. The inlet of the computational domain
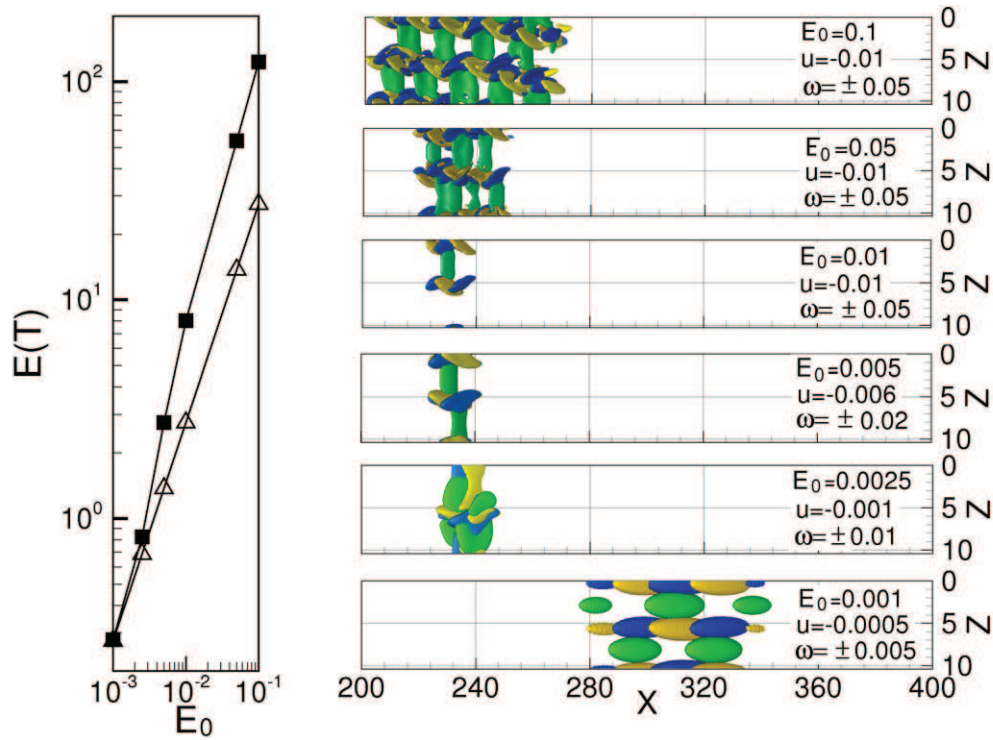
Figure 1. Optimal perturbation energy at target time $T = 75$ versus the initial energy E_0 obtained by a nonlinear (filled squares) and a linear optimization (triangles). The initial optimal perturbations obtained by the nonlinear optimization for each of the considered initial energies (filled squares) are represented on the right, for increasing initial energy from the bottom to the top. Green (gray) surfaces represent negative streamwise velocity, and yellow (light gray) and blue (dark gray) surfaces represent the negative and the positive streamwise vorticity ω, respectively. The corresponding values are indicated in the figure.

is fixed at $x_{in} = 200$. After a grid-convergence analysis, a mesh made up by $901 \times 150 \times 61$ points—stretched in the wall-normal direction—has been selected.

3. Results

Nonlinear optimizations have been performed for several initial energies, target times and Reynolds numbers. The filled squares in figure 1 are the values of the optimal energy at target time $T = 75$ and $Re = 610$, computed for $0.001 \leqslant E_0 \leqslant 0.1$. The triangles indicate the optimal energy at the same target time obtained by a linear optimization. The nonlinear optimization attains energy values that are much larger than the corresponding linear ones. The dependence of the shape of the nonlinear optimal perturbation on E_0 is shown on the right frames of figure 1. For the lowest initial energy value, the perturbation is similar to that obtained by the linear optimization (Cherubini *et al* 2010); it is characterized by elongated vortices aligned along x, localized in the middle of the domain. For $E_0 \leqslant 0.005$, with increasing initial energy, the shape of the optimal perturbation changes remarkably, moving close to the inlet and decreasing its streamwise size. For higher values of E_0, the shape of the perturbation changes slightly, being characterized by alternating vortices inclined
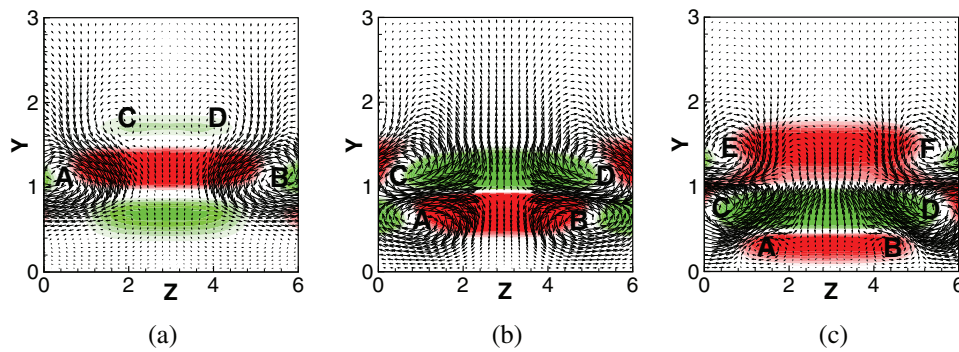
4

Figure 2. Velocity components of the initial optimal perturbation obtained for $Re = 610$, $T = 75$ and $E_0 = 0.01$, in the planes $x = 224$ (a), $x = 228$ (b) and $x = 232$ (c). Red and green contours indicate the positive and the negative streamwise disturbance velocity, respectively; vectors represent the wall-normal and the spanwise disturbance velocity components.

with respect to the streamwise direction. It is interesting that the same *basic building block* is obtained for initial energies larger than $E_0 = 0.005$, in some cases duplicated one or more times along x and/or z. The structure of the *basic building block* obtained for $E_0 = 0.01$ is shown in figure 2 on three x=constant planes. One can identify three pairs of vortices ($A–B$, $C–D$ and $E–F$) inclined with respect to the wall-normal and the streamwise direction, along regions of alternating low- and high-momentum. The upstream tilting with respect to the wall-normal direction is linked to the Orr mechanism, which is observed also in the linear optimal case, as described by Cherubini *et al* (2010). On the other hand, spanwise tilting is not observed in the linear case, in which the optimal perturbations are characterized by elongated vortices perfectly aligned with the streamwise direction (see also the bottom frame of figure 1). A similar basic structure is obtained for different target times, Reynolds number, and domain lengths; in all cases a *nonlinearity threshold* value of the initial energy exists, beyond which the optimal disturbance is found to be composed by one or more pieces of the same *basic building block* (clearly represented in the third frame from the top in figure 1 (right)). We thus define this building block as the *minimal seed* perturbation, i.e. the smallest flow structure capable of inducing the largest energy growth over a short time.

It is now interesting to determine whether and how these optimal perturbations lead the flow to turbulence. This has been done using direct numerical simulations initialized by the optimal perturbations. Computations have been performed in a domain ten times longer in x, in order to follow the flow evolution for a sufficiently long time before the disturbance wave packet leaves the domain, where a convective outflow boundary condition has now been enforced. Figure 3 provides the time evolution of the energy obtained by computations initialized with the nonlinear optimal perturbations (upper frame) and with the disturbances obtained by a linear optimization (lower frame), for different initial energies. For $E_0 = 0.001$ and $E_0 = 0.0025$, both the initial optimal perturbations decay. For $E_0 = 0.005$, $E_0 = 0.01$ and $E_0 = 0.05$, the flow re-laminarizes when initialized with the linear optimal perturbation, whereas the nonlinear optimal perturbation triggers transition, as suggested by the decay/growth of the perturbation energy, and verified by measuring the values of the skin-friction coefficient at $t = 500$, which approach those typical of laminar/turbulent flows, respectively. Thus, for such values of the initial energy, the nonlinear optimal perturbation lies in the basin of attraction of the turbulent flow, whereas the linear one remains in the basin of attraction of the laminar fixed point. The presence of the edge of chaos between $E_0 = 0.0025$
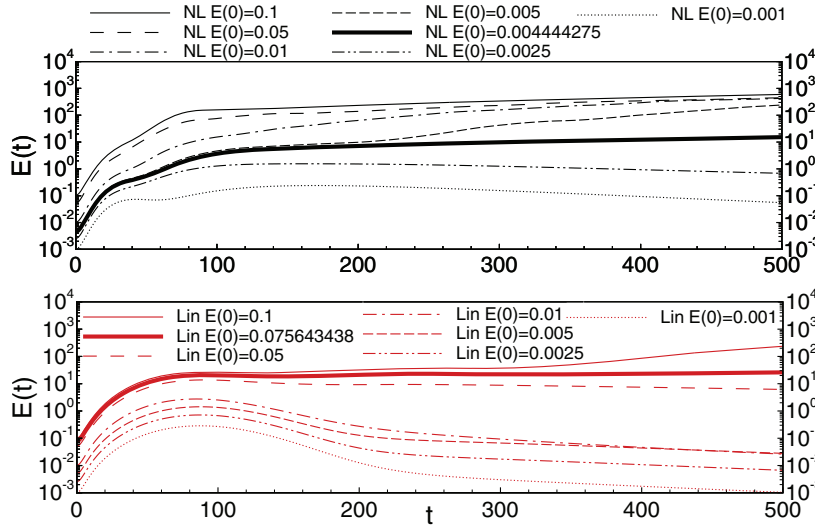
Figure 3. Evolution of the energy in time, obtained by DNS initialized with the nonlinear (top frame) and linear (bottom frame) optimal perturbation for different values of the initial energy. The thick lines are the trajectories which approach saddle points on the edge of chaos.

and $E_0 = 0.005$ (cf figure 3, top frame) thus explains the sharp difference in the shape of the optimal perturbations shown in figure 1. For larger initial energy, $E_0 = 0.1$, both the linear and nonlinear optimals are able to provoke breakdown to turbulence. This means that the linear optimal perturbation can reach the turbulent side of the laminar–turbulent boundary only for an initial energy about 20 times larger than that sufficient in the nonlinear optimal case.

The scenario of transition induced by nonlinear optimal perturbations is dramatically different from that observed for linear optimal ones. It is known that the streamwise structures constituting the linear optimal disturbances experience transition by sinuous and varicose secondary instability of the streaks induced by the initial streamwise vortices (Andersson *et al* 2001, Cherubini *et al* 2010). On the other hand, the short, streamwise-inclined vortical structures found here bypass this particular secondary instability mechanism, and provoke rapid transition, via the following sequence of events.

1. Tilting and amplification of the initial minimal seed by means of the Orr mechanism.
2. Transport of the base flow momentum by the disturbance (lift-up) along the inclined vortices, resulting in a staggered array of elongated inclined vortices on the flanks of a low-streamwise-momentum region.
3. Vortex tilting due to the interaction of the perturbation with itself, generating Λ-shaped structures of slow and fast fluids and sustaining the initial inclination of the vortices.
4. Vortex stretching by the mean flow, resulting in the creation of Λ-vortices of finite amplitude.
5. Redistribution of the vorticity due to nonlinear mixing, inducing the creation of a spanwise vorticity zone (the arch) connecting two neighboring vortex structures, constituting a main hairpin vortex.
6. Breakdown of the main hairpin and the formation of a hairpin train.

The release of smaller vortices from the main hairpin generates new, localized inclined structures, similar to those seen at larger scale, thus allowing for the cycle to repeat over
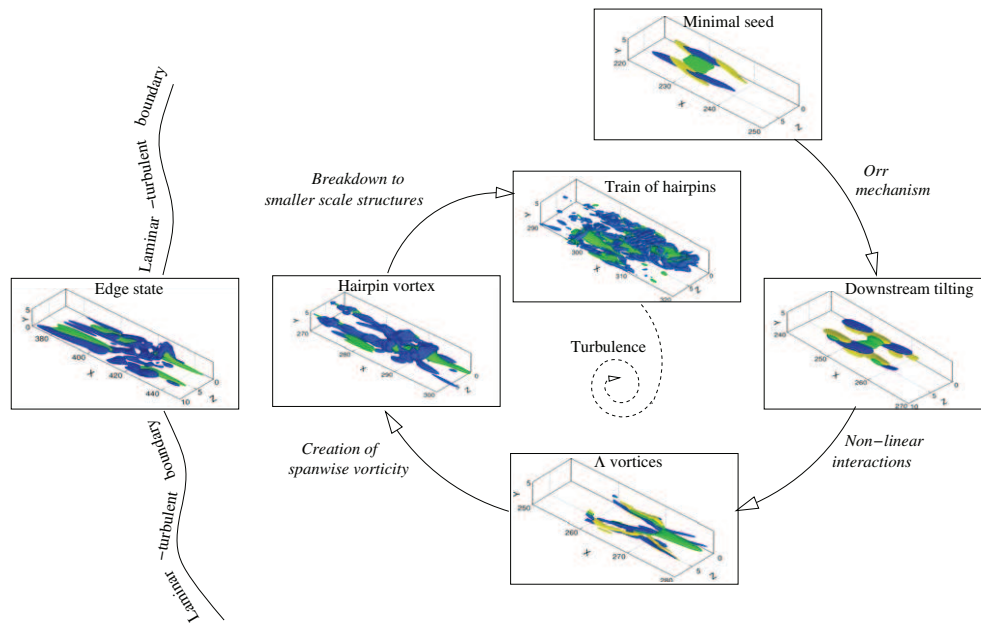
Figure 4. Sketch of the cycle of transition and disturbance-regeneration for the boundary-layer flow. The iso-surfaces in the figures (following the cycle, up to the caption 'Λ-vortices') represent the negative streamwise component of the perturbation velocity (green) and the positive and the negative streamwise disturbance vorticity (yellow and blue, respectively). In the last two frames of the spiraling curve, the green regions still represent patches of low streamwise perturbation velocity, while isosurfaces of the *Q*-criterion have been plotted in blue to visualize regions of intense vorticity. On the left, the edge structure at $t = 300$ is represented; it is obtained by initializing the simulation with the minimal seed of initial energy $E(0) = 0.004\,444\,275$.

faster (smaller) time (space) scales. The regeneration cycle briefly outlined here is sketched in figure 4 (right) and described in greater detail by Cherubini *et al* (2011a). A similar scenario of transition has been observed in direct simulations in the presence of high-amplitude free-stream turbulence by Wu and Moin (2009) and Ovchinnikov *et al* (2008), whereas a different path to turbulence was observed in previous numerical studies which employed lower-amplitude initial disturbances (Brandt *et al* 2004). The fact that the present transition scenario is triggered by finite-amplitude disturbance indicates that the underlying mechanisms are nonlinear.

In parallel flows it has been conjectured that the random walk of the system's trajectory is influenced by the relative attraction exerted by so-called exact coherent states (see, e.g., Waleffe (1998) for the case of the Couette flow). For the case of the boundary layer, we expect the trajectory of the flow to be also influenced by a relative attractor, living in the phase space on the boundary that separates the laminar from the turbulent basins of attraction. In order to establish whether the purely nonlinear route to transition initiated by the minimal seed is linked to the presence of such an attractor, we compute the (reduced) phase-space trajectories which closely follow, for a long enough time, the laminar–turbulent edge in the boundary layer. Thus, we choose as the initial condition the *minimal seed* in the third frame from the top of figure 1, and perform several bisections on the initial energy value following the procedure of Skufca *et al* (2006). The perturbation on the edge of turbulence has been extracted at different times during the simulation (cf the thick lines in figure 3). The left part
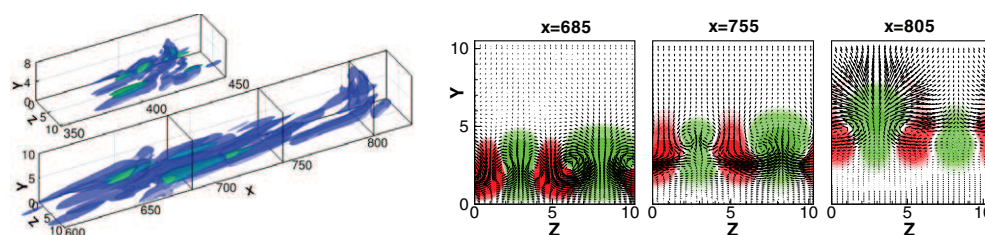
Figure 5. Snapshots of the streamwise component of the perturbation (green) and of the
Q-criterion (blue) on the laminar-turbulent boundary at $t = 300$ and $t = 700$ (top and bottom
frames on the left, respectively), and slices of the latter on the $x = $ constant planes indicated in
the figure (frames on the right): red and green contours indicate the positive and the negative
streamwise disturbance velocity, respectively; vectors represent the wall-normal and the spanwise
disturbance velocity components.

of figure 5 shows the surfaces of negative streamwise velocity components (green) and of the
Q-criterion (blue), identifying the vortical structures at $t = 300$ (top) and $t = 700$ (bottom).
The disturbance is characterized by a main hairpin vortex placed at the leading edge of the
perturbation packet, encapsulating a low-speed streak; other inclined vortices and streaks trail
the leading structure. The whole edge structure increases in size as it is convected downstream
by the mean flow, and appears to maintain a self-similar shape. In fact, normalizing the
abscissa with respect to the center of mass of the packet, computed on the basis of the local
perturbation energy, we recover a wave packet which maintains almost the same shape as
it evolves in time. Such a wave packet is characterized by structures presenting a symmetry
with respect to the wall-normal direction, as shown on three different $x = $ constant planes
in figure 5 (right frames), meaning that the streaks are undergoing oscillations of varicose
type. One can also observe that the low- and high-momentum zones at the leading edge of the
wave packet are placed quite away from the wall, and move closer to the wall at the trailing
edge. This is related to the finite inclination of the wave packet with respect to the streamwise
direction, a feature typical of turbulent spots in boundary-layer flows.

The presence of the slowly varying flow structure described above, living on the
laminar–turbulent boundary, suggests the existence of at least one relative attractor embedded
in the edge surface. This relative attractor is likely a chaotic saddle which repels any flow
which lies outside the bounding surface, influencing their route toward turbulence. Indeed,
depending on its initial energy and shape, the perturbation may spend a considerable amount
of time wandering around the relative attractor on the edge, or its route to turbulence may
be strongly deviated when passing in the neighborhood of the edge state. To analyze the
influence of the relative attractor on the perturbation trajectories, we track the trajectories of
several disturbances in an appropriately chosen phase space. For the case of parallel flows
such as plane Couette flows (Wang *et al* 2007), the dissipation rate and the energy input
are usually chosen as state variables, both based on L_2 norms. In the present case, due to
the non-parallelism of the flow, an L_∞ norm appears appropriate. Therefore, following the
theoretical work of Waleffe (1997), the maximum values of the streamwise and wall-normal
components of the velocity are chosen as state variables. Figure 6 provides the trajectories
in this reduced phase space (Cherubini *et al* 2011b) of nonlinear optimal perturbations with
different initial energy (the ones also used in figure 3, top frame). The origin (corresponding
to zero disturbance velocity with respect to the laminar Blasius solution) is the laminar
attractor; the turbulent attractor is localized on the top right, for values of the perturbation
velocity components around $u \approx 0.7$, $v \approx 0.3$; the relative attractor on the edge is the looping
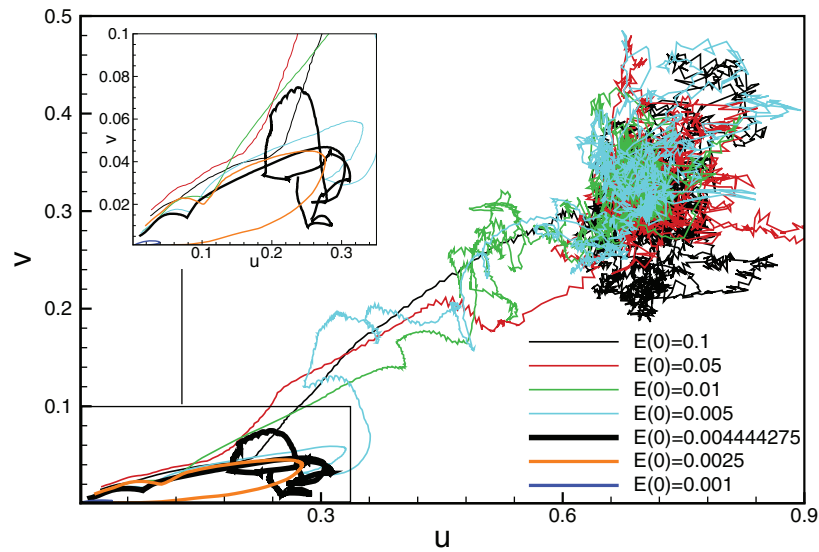
Figure 6. Trajectories in the phase space spanned by the maximum values of the streamwise and wall-normal components of the perturbation velocity, for simulations initialized by the nonlinear optimal perturbations with initial energies indicated within the frame. The trajectories have been followed up to $t = 500$.

trajectory represented by the black thick line and is localized around $u \approx 0.25$, $v \approx 0.045$ (cf also the inset in the figure). One can note the more complex structure of the turbulent attractor with respect to that of the relative chaotic attractor on the laminar–turbulent boundary, associated with lower amplitude levels. The initial perturbation having smallest initial energy ($E_0 = 0.001$, blue line) leads very rapidly to the laminar state, whereas the nonlinear optimal perturbation having largest initial energy ($E_0 = 0.1$, black thin line) brings rapidly the flow towards turbulence. On the other hand, optimal perturbations having a smaller initial energy, but larger than the nonlinearity threshold ($0.005 \leqslant E_0 \leqslant 0.05$, represented by the red, green and light blue thin lines, respectively) present a slower path to transition, spending some time wandering in a region of the phase space in between the laminar and the turbulent attractors. In particular, the initial perturbations which are closer (in an energy norm) to the laminar–turbulent boundary, namely the ones for $E_0 = 0.0025$ and $E_0 = 0.005$, represented by the light blue and orange lines, are strongly deviated by the relative attractor on the edge (black thick line), eventually leading to the laminar fixed point (through a homoclinic cycle) or to the turbulent attractor, respectively, after having closely approached the edge for a certain amount of time. The length of the path leading to the turbulent attractor appears to be correlated to the proximity of the perturbation to the edge of turbulence. Initial perturbations which pass close (in the energy norm) to the laminar–turbulent boundary may be affected by the presence of the relative attractor, and evolve in time towards hairpin-shaped structures similar to those characterizing the edge state.

Furthermore, there are clues as to the existence of other relative attractors, since some of the trajectories appear to be locally attracted and deviated towards other regions of phase space: for instance, the inset in figure 6 shows clearly that all trajectories for E_0 in the interval [0.0025, 0.005] display a cusp (possible indication of an unstable fixed point), which corresponds in figure 3 (top frame) to the kink in the energy curve for t around 50. Also, observation of the green line ($E_0 = 0.01$) at $u \approx 0.5$, $v \approx 0, 25$, induces
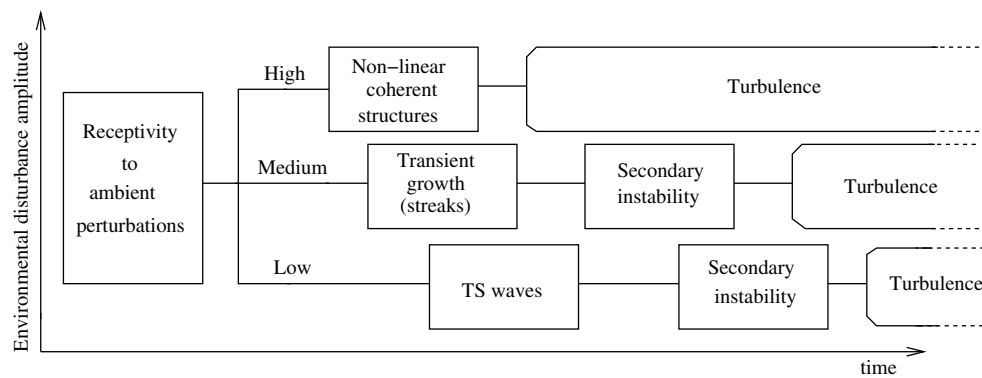
9

Figure 7. Sketch of the different scenarios of transition in a boundary layer.

us to speculate on the existence of a second chaotic saddle, similar to what was found by several authors in Couette and pipe flows (see, e.g., Gibson et al 2009, Pringle et al 2009).

The minimal seed perturbation, which is the smallest flow structure able to induce large energy growth over short times, is found to lead the flow close to the relative laminar–turbulent attractor following a very fast path. With reference to figure 4, after the flow has approached the stable manifold of the turbulent attractor near the edge state, it experiences breakdown, inducing new smaller-scale vortical structures, eventually yielding a hairpin train through a sequence of events at smaller spatial scales—similar to that sketched in the figure for the large-scale initial disturbance. It is thus suggested that a hairpin-regeneration cycle exists at each local scale, until the limiting scales defined by viscous dissipation. This scenario of transition accounts for the preponderance of hairpin structures in transitional boundary layers, as observed in both experiments (Boiko *et al* 2012) and numerical studies (Wu and Moin 2009).

4. Summary

A purely nonlinear route to transition exists for the boundary-layer flow, which is optimally initiated by the *minimal seed* perturbation and evolves in time towards Λ and hairpin structures. Such a nonlinear route to turbulence is very different from the classical ones initiated by either streamwise vortices or the Tollmien–Schlichting waves (see the sketch in figure 7); the present path to turbulence is influenced by the presence of a relative attractor embedded in the edge of chaos. Such an attractor is characterized by a coherent flow structure made of a main hairpin vortex surrounded by streaks, which maintains a quasi self-similar aspect as it is convected downstream. We have shown that a preferential route exists connecting the perturbed laminar state with the turbulent one and approaching an exact coherent state (and possibly more than one). It is the aim of our future work to identify the other saddle points that may exist and possibly influence transition.

Acknowledgments

References

Andersson P, Brandt L, Bottaro A and Henningson D S 2001 *J. Fluid Mech.* **428** 29–60
Biau D and Bottaro A 2009 *Phil. Trans. R. Soc.* A **367** 529–44
Boiko A V, Dovgal A V, Grek G R and Kozlov V V 2012 *Physics of Transitional Shear Flows* (Berlin: Springer)
Brandt L, Schlatter P and Henningson D S 2004 *J. Fluid Mech.* **517** 167–98
Cherubini S, De Palma P, Robinet J C and Bottaro A 2010 *Phys. Rev.* E **82** 066302
Cherubini S, De Palma P, Robinet J C and Bottaro A 2011a *J. Fluid Mech.* **689** 221–53
Cherubini S, De Palma P, Robinet J C and Bottaro A 2011b *Phys. Fluids* **23** 051705
Cherubini S, Robinet J C, Bottaro A and De Palma P 2010 *J. Fluid Mech.* **656** 231–59
Duguet Y, Brandt L and Larsson B R J 2010 *Phys. Rev.* E **82** 026316
Eckhardt B, Schneider T M, Hof B and Westerweel J 2007 *Annu. Rev. Fluid Mech.* **39** 447–68
Faisst H and Eckhardt B 2003 *Phys. Rev. Lett.* **91** 224502
Farrell B 1988 *Phys. Fluids* **31** 2093–102
Gibson J F, Halcrow J and Cvitanović P 2009 *J. Fluid Mech.* **638** 243
Hof B, van Doorne C, Westerweel J, Nieuwstadt F, Faisst H, Eckhardt B, Wedin H, Kerswell R and Waleffe F 2004
     Science **305** 1594–8
Luchini P 2000 *J. Fluid Mech.* **404** 289–309
Marquet O, Sipp D, Chomaz J M and Jacquin L 2008 *J. Fluid Mech.* **605** 429–43
Nagata M 1997 *Phys. Rev.* E **55** 2023
Ovchinnikov V, Choudhari M M and Piomelli U 2008 *J. Fluid Mech.* **613** 135–69
Polak E and Ribière G 1969 *Rev. Fr. Inform. Rech. Oper.* **3** 35–43
Pringle C C T, Duguet Y and Kerswell R 2009 *Phil. Trans. R. Soc.* A **367** 457–72
Pringle C C T and Kerswell R 2010 *Phys. Rev. Lett.* **105** 154502
Schneider T M, Gibson J F and Burke J 2010 *Phys. Rev. Lett.* **104** 104501
Skufca J D, Yorke J and Eckhardt B 2006 *Phys. Rev. Lett.* **96** 174101
Verzicco R and Orlandi P 1996 *J. Comput. Phys.* **123** 402–14
Viswanath D and Cvitanovic P 2009 *J. Fluid Mech.* **627** 215
Waleffe F 1997 *Phys. Fluids* **9** 883–901
Waleffe F 1998 *Phys. Rev. Lett.* **81** 4140–3
Wang J, Gibson J F and Waleffe F 2007 *Phys. Rev. Lett.* **98** 204501
Wu X and Moin P 2009 *J. Fluid Mech.* **630** 5–41